有机化学 DOI: 10.6023/cjoc202108017 研究论文
Chinese Journal of Organic Chemistry ARTICLE

基于 9,9'-螺二芴和萘的纯碳氢主体材料

郑 琦 文 亚 屈扬坤 朱元皓 冯敏强* 蒋佐权*
(苏州大学功能纳米与软物质研究院 江苏省碳基功能材料与器件重点实验室 江苏苏州 215123)

摘要 利用磷光有机发光二极管的主客体掺杂结构有助于避免三重态激子浓度猝灭, 从而提高器件性能. 9,9'-螺二芴(SBF)及其衍生物具有独特的正交构型和刚性骨架, 具有高玻璃化转变温度、高三线态能级和用作主体材料的潜力. 通过引入萘环合成并表征了两种基于 SBF 的纯碳氢化合物(PHC)磷光发光器件的主体材料, 命名为 1,4-SBF-Nap 和 1,8-Oct-Nap. 其中, 1,8-Oct-Nap 分子存在一个有趣的环化反应, 形成八原子环结构而不是一般的 SBF. 以 $Ir(MDQ)_2(acac)$为客体, 成功制备了基于这两种主体的红光器件, 最大外量子效率(EQE)分别为 15.0%和 13.7%, 证明 PHC 主体材料在设计上的多样性.

关键词 有机发光二极管; 主体材料; 9,9'-螺二芴; 萘; 八元环

Pure Hydrocarbon Host Materials Based on 9,9'-Spirobifluorene/Naphthalene Hybrid

Zheng, Qi Wen, Ya Qu, Yangkun Zhu, Yuanhao
Fung, Mankeung* Jiang, Zuoquan*
(*Institute of Functional Nano & Soft Materials*, *Jiangsu Key Laboratory for Carbon-Based Functional Materials & Devices*, *Soochow University*, *Suzhou*, *Jiangsu 215123*)

Abstract The utilization of host-guest doped structure of phosphorescent organic light-emitting diodes helps avoid the triplet exciton concentration quenching, thus improve the device performance. 9,9'-Spirobifluorene (SBF) and its derivatives with a unique orthogonal configuration and rigid framework, exhibit high glass transition temperature, high triplet energy levels, and potential to be used as host materials. In this work, two types of SBF-based pure hydrocarbon (PHC) phosphorescent light-emitting device host materials were synthesized and characterized by introducing naphthalene, named 1,4-SBF-Nap and 1,8-Oct-Nap. 1,8-Oct-Nap has an interestingly cyclized cites and resulting in an octatomic ring structure instead of normal SBF. Co-evaporating with bis(2-methyldibenzo[f,h]quinoxaline)(acetylacetonate)iridium(III) ($Ir(MDQ)_2(acac)$), the red-light devices based on these two hosts were successfully fabricated. The maximum external quantum efficiencies (EQE) were 15.0% and 13.7% for 1,4-SBF-Nap and 1,8-Oct-Nap, respectively. The diversity of the PHC host materials can be expanded by the utilization of naphthalene.

Keywords organic light-emitting diode; host; 9,9'-spirobifluorene; naphthalene; octatomic ring

1 Introduction

In recent years, organic light-emitting diodes (OLEDs) have been used in displays and solid-state lighting, owing to their superior characteristics. However, there are still many restrictions for the commercial development of OLED, such as the cost, efficiency, and lifetime. Since reported in 1998 by Forrest *et al.*,[1] phosphorescent organic light-emitting diodes (PhOLEDs) are maturer than fluorescent organic light-emitting diodes (FOLEDs). Compared with traditional FOLEDs, PhOLEDs can harvest both singlet and triplet excitons by efficient intersystem crossing from the lowest singlet excited state (S_1) to triplet excited state (T_1), thus theoretically reach 100% internal quantum efficiency (IQE).[2] In PhOLEDs, the participation of a suitable host can enhance the device performance by preventing triplet-triplet annihilation (TTA), triplet-polaron quenching (TPQ), and the reverse energy transfer from the emitter to the host.[3] The reverse energy transfer from T_1 of the phosphorescent material to that of the hosts has a detrimental

* Corresponding authors. E-mail: mkfung@suda.edu.cn; zqjiang@suda.edu.cn
Received August 13, 2021; revised September 14, 2021; published online October 14, 2021.
Project supported by the National Natural Science Foundation of China (Nos. 51773141, 51873139, 61961160731, 51821002).
国家自然科学基金(Nos. 51773141, 51873139, 61961160731, 51821002)资助项目.

effect on the efficiency of the device. Therefore, the host materials should possess higher T_1 energy than the phosphorescent materials. In addition, good charge carrier transport properties, as well as good thermal and morphologic stability, are required for the hole-electron recombination process and device stability, respectively.[4]

Most host materials have heteroatoms groups, such as carbazole,[5] phosphine oxide,[6] quinolinophenothiazine,[7] pyridine,[8,9] *etc*., to enrich material diversity and function to meet various demands. However, Qiao *et al*.[10,11] have found that C—S, C—P, and C—N bonds are significantly weaker than C—C bond, which decrease the device stability. Therefore, pure hydrocarbon (PHC) hosts without any heteroatoms are thus developed.[12] For organic semiconductors, the introduction of spiro structure improves the thermal and morphological stability, owing to its steric hindrance characteristics.[13,14] Several groups including us develop series of PHC materials based on spiro structure include 9,9'-spirobifluorene (SBF).[13-18] For example, our group proposed the advantages of C1 connection SBF in 2018,[19] such as keeping a high E_T, inducing excellent thermal properties and so on. Poriel and coworkers developed a serious of PHC hosts based on one or several SBF and phenyl groups, such as 2-Ph-SBF and 4-Ph-SBF.[20] They also reported some dihydroindenofluorene with three different phenyl linkages (*para/meta/ortho*)[21] and two different ring bridge arrangements (*anti/syn*).[22]

Besides classic benzene ring, naphthalene is the simplest PHC fused ring, but its application in host materials is seldom studied.[23] In this study, two PHC host materials, 1,4-di(9,9'-spirobi[fluoren]-1-yl)naphthalene (1,4-SBF-Nap) and 1,8-di(9,9'-spirobi[fluoren]-1-yl)naphthalene (1,8-SBF-Nap), were designed based on naphthalene and SBF. Interestingly, the second one exhibited an unexpected cyclization reaction site, owing to its steric effect, thus an octatomic ring structure 1,8-Oct-Nap was gotten. From a synthetic point of view, we accidentally obtained an octatomic ring structure in the SBF host systems, which leaded to a more rigid structure. Using these two materials as host and bis(2-methyldibenzo[f,h]quinoxaline)(acetylacetonate)iridium(III) ($Ir(MDQ)_2(acac)$) as the guest, the red emission devices were successfully fabricated, which showed maximum EQEs of 15.0% and 13.7% for 1,4-SBF-Nap and 1,8-Oct-Nap, respectively, compared with that of 1,3-bis(carbazol-9-yl)benzene (mCP) as the host (13.8%) under the same conditions. Furthermore, the introduction of naphthalene into the PHC host materials expands the diversification of the PHC host materials.

2 Results and discussion

The synthetic routes of 1,4-SBF-Nap and 1,8-Oct-Nap are shown in Scheme 1. Compounds **1** and **2** were synthesized by using a Suzuki-Miyaura coupling reaction. Then, the final products were successfully afforded by following a lithium-halogen exchange, nucleophilic addition, and Friedel-Crafts cyclization. Both final products were characterized by ^{1}H NMR, ^{13}C NMR, and mass spectroscopies. The structure of compound **4** was fixed when occupied the electrophilic reaction since it reacted under −78 ℃, which means the temperature cannot change the spatial structure. In order to explain why octatomic ring formed instead of SBF, the energies of possible diol intermediates with different spatial structures of 1,8-Oct-Nap and result in four possible structures named IM-1-4 caused by different choices of same or opposite directions for the hydroxyl group and vertical or parallel positions of the terminal benzene in the diphenyl group to the neighbor fluorene as a) in Figure 1, using the density functional theory (DFT) calculation.[24] The IM-4, with the lowest energy state settled as 0, has a configuration of π-π interaction owing to the parallel position of the terminal benzene in the diphenyl group to the neighbor fluorene, which means it tends to cyclize between two fluorenes and thus result in the octatomic ring. We also calculated the energies of the possible structures named IM-5 and IM-6 with H_2O, when the octatomic ring has formed on one side. However, once one side of an octatomic ring is formed, the other side can only build SBF group because of the structural limitation.

The density functional theory (DFT) and time-dependent DFT (TD-DFT) calculations were performed to analyze the energy levels and the distribution of electrons and holes of the molecules. As shown in Figure 2, the highest occupied molecular orbital (HOMO) and the lowest unoccupied molecular orbital (LUMO) of 1,4-SBF-Nap are mainly located on the naphthalene group. The distribution of HOMO for 1,8-Oct-Nap is mainly on the naphthalene group and partially on the neighboring benzene part of SBF group, and its LUMO is mainly located on the naphthalene group and partially on the neighboring benzene part of the other side, where no cyclization reaction occurred. The calculated HOMO and LUMO for 1,4-SBF-Nap and 1,8-Oct-Nap are −5.95/−1.08 and −5.71/−1.38 eV, respectively, which exhibits differences caused by their various distribution on naphthalene or octatomic ring. Also, the electron-hole analyses of the S_1 and T_1 states were calculated for both materials (Multiwfn[28] and VMD[29]). For 1,4-SBF-Nap, the electron and hole distributions of the S_1 state are located on the naphthalene unit and two diphenyl groups that do not connect with naphthalene directly, respectively. However, the electron and hole distributions of the T_1 state are mainly located on the naphthalene unit. As for 1,8-Oct-Nap, the electron-hole distributions of S_1 and T_1 states are mainly located on the naphthalene unit and partially on the neighboring benzene part that has not been cyclized. The difference of energy of S_1 state for 1,4-SBF-Nap (3.88 eV) and (3.43 eV) is a little higher than that of T_1 state (2.17 eV for 1,4-SBF-Nap and 1.96 eV for 1,8-Oct-Nap), because of their different levels of distribution.

The UV-vis absorption spectra, fluorescence spectra, and phosphorescence spectra of both molecules are shown in Figure 4. The UV-vis absorption spectra and fluorescence spectra of molecules were measured in toluene (10^{-5}

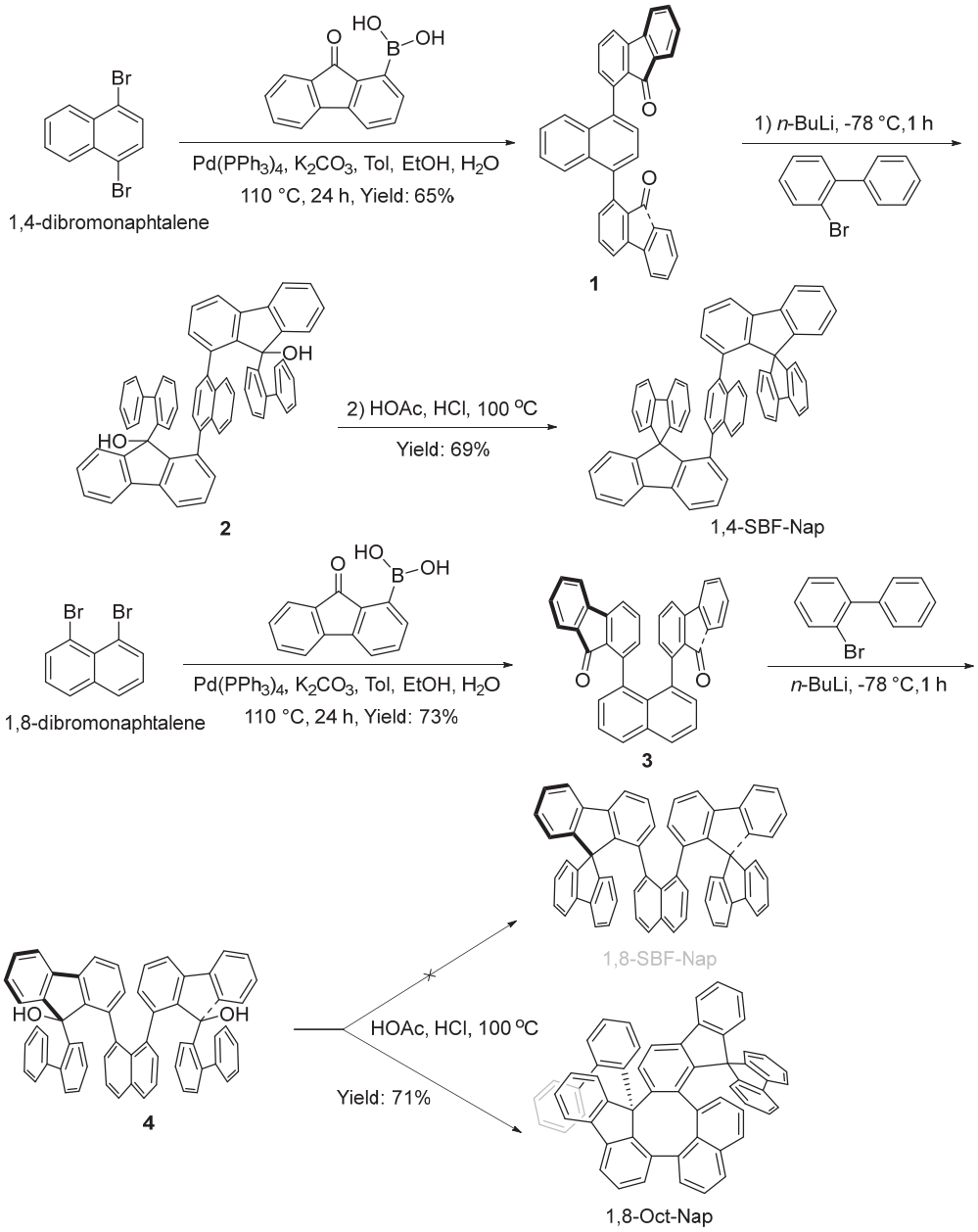

Scheme 1 Synthetic routes of 1,4-SBF-Nap and 1,8-Oct-Nap.

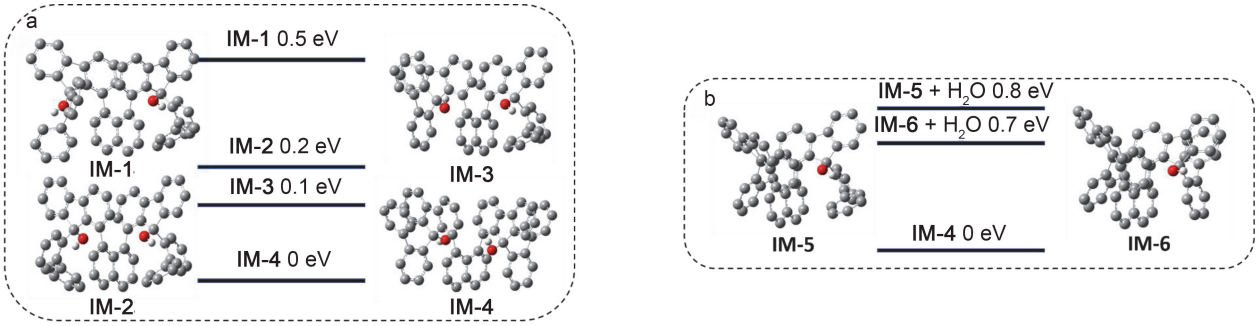

Figure 1 Theoretical calculations of the possible intermediate spatial structures of 1,8-Oct-Nap using DFT[24] (ground states) at the pbe0 [25] (em=gd3bj)[26]/def2svp[27] level

mol/L) at room temperature, while the phosphorescence spectra were measured at 77 K. All photophysical data of these two hosts are summarized in Table S1. Both materials exhibit sharp absorption at *ca.* 280 and 310 nm, which

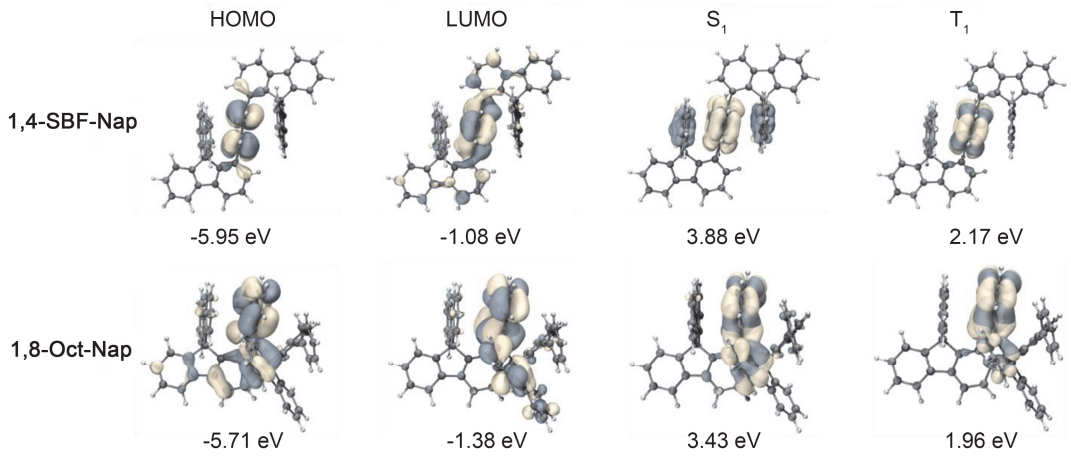

Figure 2 Theoretical HOMO/LUMO energy levels and distributions, singlet and triplet excitation energies, and electron-hole analysis of singlet and triplet excited states, for 1,4-SBF-Nap and 1,8-Oct-Nap using DFT (ground states) at the pbe0[25] (em＝gd3bj)[26]/def2svp[27] level and TD-DFT (excited states) at the cam-b3lyp[30] (em＝gd3bj)[26]/def2svp[27] level

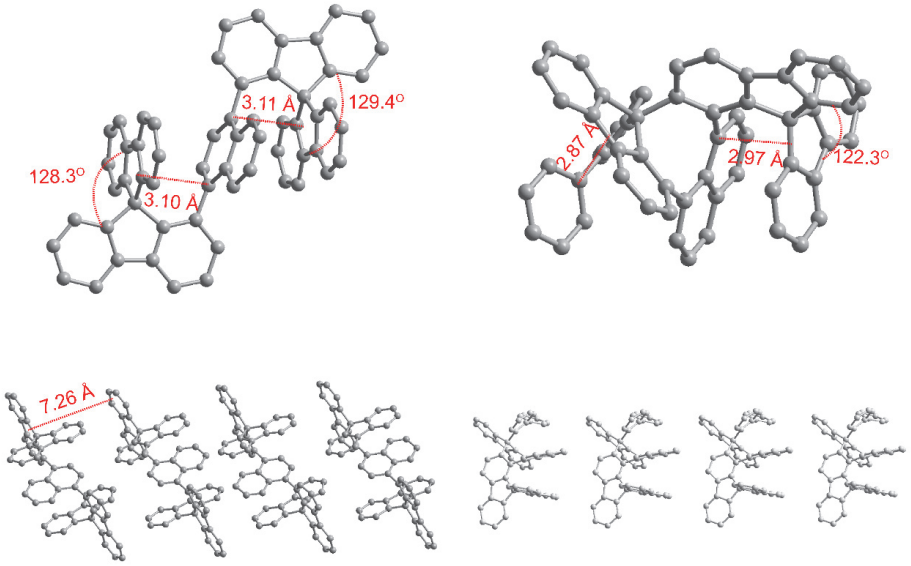

Figure 3 Crystal structures and crystal packing modes of 1,4-SBF-Nap and 1,8-Oct-Nap

can be attributed to the SBF group. The strong absorption band observed at 250～330 nm is owing to the π-π* transitions of the conjugated structure. The absorption edges of 1,4-SBF-Nap and 1,8-Oct-Nap are 317 and 320 nm, respectively. According to the fluorescence spectra, 1,4-SBF-Nap exhibits a sharp peak value of 354 nm, while 1,8-Oct-Nap has a sharp peak of 365 nm. The S_1 and T_1 energy levels were measured from the highest energy peak of the fluorescence and phosphorescence spectra, respectively. 1,4-SBF-Nap has an S_1 value of 3.44 and a T_1 value of 2.54 eV, while 1,8-Oct-Nap holds an S_1 value of 3.34 eV and a T_1 value of 2.52 eV. By comparing the calculated results with this, for S_1 energy, the error range of 1,4-SBF-Nap is higher than that of 1,8-Oct-Nap, but the T_1 energy is the opposite. The overall trend of the calculation results and measurement data are matched.

The electrochemical properties of 1,4-SBF-Nap and 1,8-Oct-Nap have been testified in CH_2Cl_2 (oxidation) Bu_4NPF_6 (0.1 mol/L) using cyclic voltammetry (CV), which have distinct oxidation behaviors as Figure 5 shows. Their voltammograms show different first monoelectronic wave and irreversible process. The onset of oxidation potentials (E_{ox}) of 1.48 and 1.18 eV are observed for 1,4-SBF-Nap and 1,8-Oct-Nap, respectively. The HOMO energy levels are calculated of −5.76 eV of 1,4-SBF-Nap and −5.45 eV of 1,8-Oct-Nap, which have a little difference with the calculated results but same trends. The LUMO energy levels were determined by combining the HOMO levels and the optical band gap levels. The LUMO energy levels of 1,4-SBF-Nap and 1,8-Oct-Nap are −1.89 and −1.59 eV, respectively. This kind of trend in the electrochemical properties can also be found in the device performance.

The thermal properties of 1,4-SBF-Nap and 1,8-Oct-Nap have been studied by thermogravimetric analysis (TGA) and differential scanning calorimetry (DSC) under N_2 at-

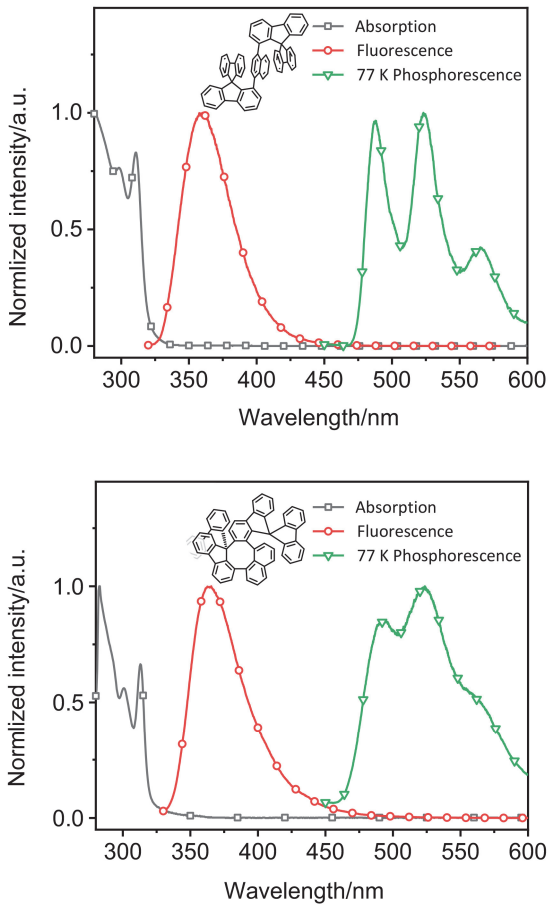

Figure 4 UV-vis absorption, fluorescence, and phosphorescent (77 K) spectra of 1,4-SBF-Nap and 1,8-Oct-Nap

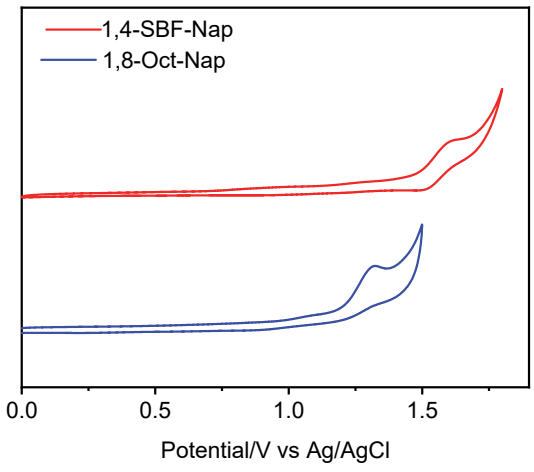

Figure 5 Cyclic voltammetry in CH_2Cl_2/[Bu_4NPF_6] 0.1 mol/L (100 mV•s^{-1}) of 1,4-SBF-Nap and 1,8-Oct-Nap

mosphere. The result shows that 1,4-SBF-Nap has the decomposition temperatures at 5% mass loss (T_d) of 408 ℃, while 1,8-Oct-Nap has a T_d of 411 ℃, which are almost the same owing to their same molecular weight. The high decomposition temperature allows these two materials to fabricate OLED devices. In DSC test, 1,4-SBF-Nap exhibited a high glass transition temperature (T_g) of 105 ℃ while 1,8-Oct-Nap did not give distinct endothermic change or peak.

The device performance of both host materials and compared mCP was tested and summarized in Figure 6 and Table 1 with the structure: indium tin oxide (ITO)/1,4,5,8,9,11-hexaazatriphenylene hexacarbonitrile (HATCN, 10 nm)/1,1-bis[4-[*N*,*N*-di(p-tolyl)amino]phenyl]-cyclohexane (TAPC, 40 nm)/tris(4-carbazolyl-9-ylphenyl)amine (TCTA, 10 nm)/Hosts: 3 wt% $Ir(MDQ)_2(acac)$ (20 nm)/4,6-bis(3,5-di(pyridin-4-yl)phenyl)-2-methylpyrimidine (B4PyMPM) (50 nm)/8-hydroxyquinolinolatolithium (Liq) (2 nm)/Al (120 nm). In the emitting layers (EML), $Ir(MDQ)_2$(acac) is bis(2-methyldibenzo[f,h]quinoxaline)(acetylacetonate)iridium(III). HAT-CN and Liq were used as hole-injection and electron-injection layers to enhance the holes and electrons injection, respectively. TAPC (HOMO *ca.* −5.5 eV) and TCTA (HOMO *ca.* −5.8 eV) materials with suitable HOMO energy levels and excellent hole mobility were selected as hole-transporting layers. B4PyMPM with LUMO energy of −7.1 eV was served as electron-transporting layer. As illustrated in Table 1, the device with 1,4-SBF-Nap exhibited a highest maximum external quantum efficiency (EQE) of 15.0%, a maximum current efficiency (CE) of 25.5 cd•A^{-1} and a maximum power efficiency (PE) of 22.3 lm•W^{-1}. In comparison, the device with 1,8-Oct-Nap has a maximum EQE of 13.7%, a CE of 21.9 cd•A^{-1} and a PE of 22.9 lm•W^{-1}; the device with mCP exhibits a maximum EQE of 13.8%, a CE of 22.6 cd•A^{-1} and a PE of 22.3 lm•W^{-1}. The device with 1,4-SBF-Nap as the host has a better performance than the other two devices, for example, its maximum EQE and luminance value, owing to its more compact crystal packing structure as Figure 3. However, the device with 1,8-Oct-Nap has similar properties with mCP, except its luminance exceeding 10^4 cd•m^{-2}.

3 Conclusions

This work reports a design strategy of the PHC host by introducing the naphthalene group with different substitution sites and conquers an unexpected octatomic ring structure caused by steric hindrance. To further explore the formation of the octatomic ring structure, the possible intermediate structures were calculated, which have π-π in-

Table 1 Summary of device performances

Host	V_{on}/V_{100}[a]/V	CE_{max}[b]/(cd•A^{-1})	PE_{max}[b]/(lm•W^{-1})	EQE_{max}[b]/%	λ_{max}[c]/nm	CIE (x, y)[c]
1,4-SBF-Nap	3.6/4.8	25.5/18.8/12.7	22.3/12.2/5.6	15.0/11.0/7.3	608	(0.61, 0.38)
1,8-Oct-Nap	3.0/4.2	21.9/14.4/9.7	22.9/10.8/5.1	13.7/9.0/6.1	608	(0.62, 0.38)
mCP	2.8/3.2	22.6/22.6/19.2	22.3/22.2/14.4	13.8/13.8/11.7	608	(0.61, 0.38)

[a] Operating voltage at onset, and 100 cd•m^{-2}; [b] The CE, PE and EQE at the maximum, 100 and 1000 cd•m^{-2}; [c] Measured at a driving current density of 5 mA•cm^{-2}.

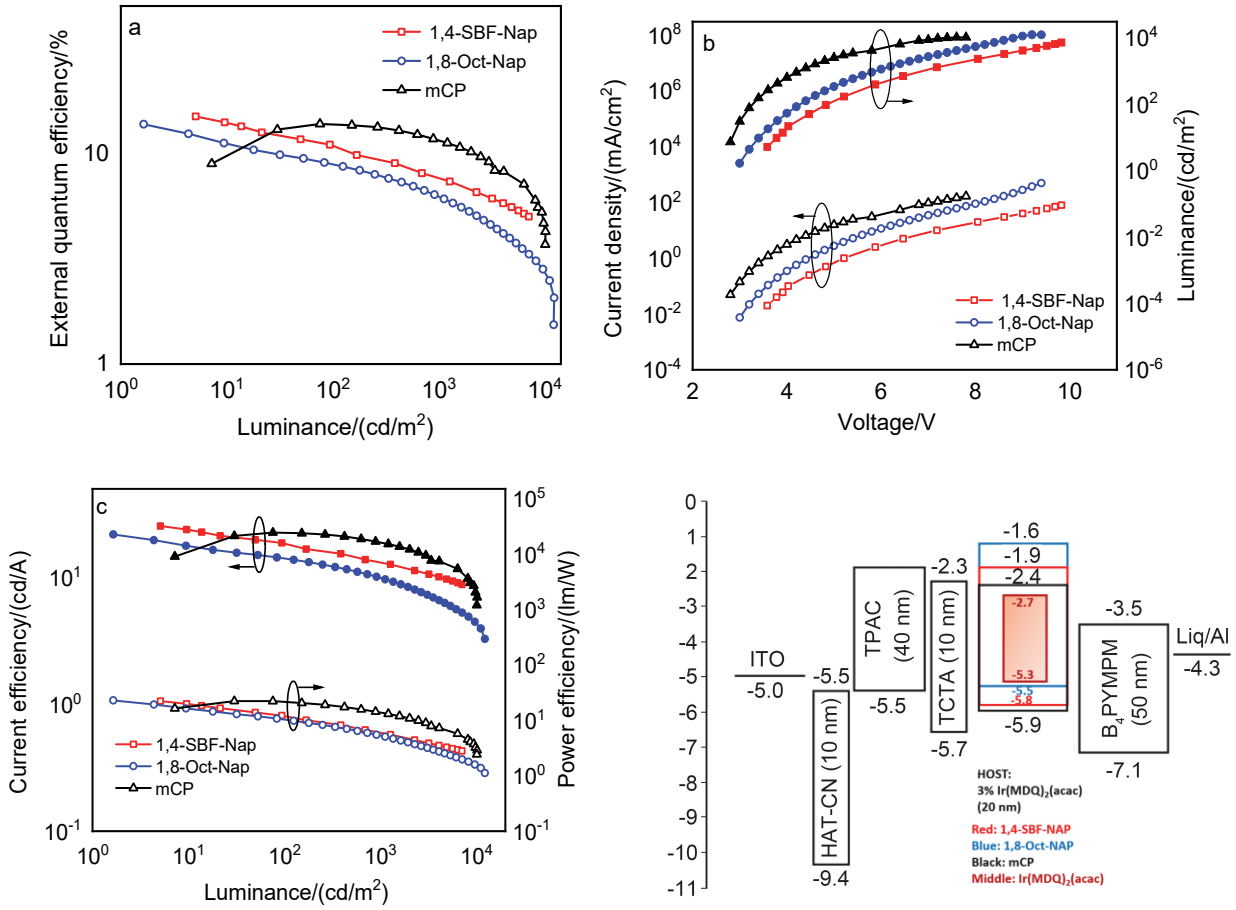

Figure 6 PhOLED device performance

PhOLED device characteristics of 1,4-SBF-Nap (red), 1,8-Oct-Nap (blue) and mCP (black). (a) EQE versus luminance characteristics; (b) current density and luminance versus driving voltage (*J*–*V*–*L*) characteristics; (c) current efficiency and power efficiency versus luminance characteristics; (d) device structures of PhOLEDs based on 1,4-SBF-Nap, 1,8-Oct-Nap, and mCP, with functional materials including HAT-CN, TAPC, TCTA, Ir(MDQ)2(acac), B4PyMPM, Liq and Al

teraction owing to the parallel position of the terminal benzene in the diphenyl group to the neighbor fluorine. The maximum EQEs of 15.0% and 13.7% of red PHOLED devices for 1,4-SBF-Nap and 1,8-Oct-Nap were obtained, respectively, which were better than or similar to the carbazole based host mCP (13.8%). This work discloses two kinds of new PHC host materials constructed by SBF and naphthalene units.

4 Experimental section

4.1 Instruments and reagents

^{1}H NMR and ^{13}C NMR spectra were performed on a Bruker 400 MHz spectrometer at room temperature. Matrix-Assisted Laser Desorption/Ionization Time of Flight Mass Spectrometry (MALDI-TOF-MS) were measured with a Bruker Autoflex II/Compass 1.0. Mass spectroscopy was performed using a Thermo Fisher ISQ Single Quadrupole GC-MS with direct probe system. High resolution mass spectra (HRMS) were recorded at the Thermo Scientific Q Exactive Combined Quadrupole Orbitrap Mass Spectrometer on a Bruker MicrO-Tof-Q II (Source Atmospheric Pressure Chemical Ionization (APCIDirectr introduction) (ASAP-Atmospheric Solids Analysis Probe) at room temperature-positive mode. Perkin Elmer Lambda 750 spectrophotometer was used to record UV-Vis absorption spectra. To record PL spectra, a Hitachi F-4600 fluorescence spectrophotometer was employed. Differential scanning calorimetry (DSC) were recorded on a METTLER TOLEDO DSC1. Thermogravimetric analysis (TGA) were recorded on a TA SDT 2960 instrument unit. Cyclic voltammetry (CV) was performed on a CH1600 voltammetric analyzer at room temperature. The crystals of STF-DPS and STFDBTS were grown by slow evaporation in dichloromethane. A Bruker D8-Venture diffractometer with a Turbo X-ray source (Mo Kα radiation, λ=0.071073 nm) was used adopting the direct-drive rotating anode technique and a CMOS detector to collected the single-crystal data.

1,4-dibromonaphtalene, 1,8-dibromonaphtalene, Pd(PPh_3)$_4$, and K_2CO_3 were purchased from commercial resources and directly used without further purification. (9-Oxo-9*H*-fluoren-1-yl)boronic acid was synthesized according to the work of Demeter *et al.*[31]

4.2 Synthesis of 1,4-SBF-Nap

A mixture of 1,4-dibromonaphtalene (0.5 g, 1.6 mmol), (9-*oxo*-9*H*-fluoren-1-yl)boronic acid (0.8 g, 3.7 mmol), $Pd(PPh_3)_4$ (0.2 g, 0.16 mmol), and K_2CO_3 (1.1 g, 8.0 mmol) in tetrahydrofuran (50 mL) and distilled water (10 mL) was refluxed overnight under argon. The mixture was then extracted with dichloromethane (50 mL) three times. The combined organic extracts were dried over anhydrous Na_2SO_4 and concentrated by rotary evaporation. The crude product was directly used without further purification to give 1,1'-(naphthalene-1,4-diyl)bis(9*H*-fluorene-9-one) (**1**) (0.50 g, 65%) as yellow solid. MS (EI) *m/z*: 484.38 $[M]^+$.

To a solution of 2-bromo-1,1'-biphenyl (0.67 g, 2.88 mmol) in tetrahydrofuran (20 mL) under argon was added *n*-BuLi (1.8 mL, 1.6 mol/L in hexane, 2.88 mmol) dropwise at −78 ℃ in a 50 mL Schlenk flask. After string for 1 h at −78 ℃, compound **1** (0.67 g, 1.38 mmol) was added in one portion. After string for 2 h at room temperature, the resulting mixture was quenched with methanol, concentrated by rotary evaporation and washed with warm methanol to give the crude solid. The crude intermediate was then dissolved in acetic acid (20 ml) and heated to 70 ℃ before 2 mL of concentrated HCl (37%) was added to the mixture which was stirred at 100 ℃ overnight. The resulting mixture was cooled down to room temperature and poured into ice water (100 mL). The precipitate was isolated by filtration and purified by column chromatography on silica gel (CH_2Cl_2/petroleum ether, V∶V=10∶1～3∶1) to give 1,4-SBF-Nap (0.72 g, 69%) as white solid. m.p. 366 ℃; ^{1}H NMR (400 MHz, Methylene Chloride-d_2) δ: 7.97 (dd, J=7.7, 1.1 Hz, 2H), 7.91 (dt, J=7.7, 1.0 Hz, 2H), 7.58 (t, J=7.5 Hz, 2H), 7.34 (td, J=7.5, 1.1 Hz, 2H), 7.20 (dt, J=7.6, 1.0 Hz, 2H), 7.08 (td, J=7.4, 1.1 Hz, 2H), 7.04～6.99 (m, 4H), 6.96 (dd, J=7.4, 1.2 Hz, 2H), 6.89 (dt, J=7.7, 0.9 Hz, 2H), 6.67～6.60 (m, 4H), 6.55～6.49 (m, 4H), 6.42 (dt, J=7.6, 0.9 Hz, 2H), 6.35～6.27 (m, 4H), 5.19 (s, 2H); ^{13}C NMR (101 MHz, CD_2Cl_2) δ: 149.27, 149.18, 146.40, 145.43, 142.51, 142.05, 141.48, 141.09, 138.53, 133.92, 130.45, 130.14, 127.76, 127.52, 127.09, 127.03, 126.99, 126.32, 125.25, 124.45, 123.57, 123.45, 123.43, 123.27, 120.03, 119.74, 119.06, 118.28, 65.73. HRMS calcd for $C_{60}H_{36}$: 756.2817, found 756.2866.

4.3 Synthesis of 1,8-Oct-Nap

The synthetic method of compound **3** is similar as compound **1** but using 1,8-dibromonaphtalene instead of 1,4-dibromonaphtalene to give crude product. The crude product was directly used without further purification to give 1,1'-(naphthalene-1,8-diyl)bis(9*H*-fluorene-9-one) (**3**) (0.57 g, 73%) as yellow solid. MS (EI) *m/z*: 484.52 $[M]^+$.

The synthetic method of 1,8-Oct-Nap is similar to that of 1,4-SBF-Nap, using compound **3** (0.57 g, 1.17 mmol) instead of compound **1** to give 0.63 g of 1,8-Oct-Nap (71%) as white solid. m.p. 345 ℃; ^{1}H NMR (400 MHz, Chloroform-*d*) δ: 7.84 (d, J=7.7 Hz, 2H), 7.64 (d, J=7.5 Hz, 2H), 7.35～7.27 (m, 4H), 7.13 (t, J=7.4 Hz, 2H), 6.99～6.86 (m, 8H), 6.78 (t, J=7.6 Hz, 2H), 6.62～6.54 (m, 4H), 6.48 (d, J=7.5 Hz, 2H), 6.34 (dd, J=7.5, 5.6 Hz, 4H), 6.30～6.21 (m, 4H), 5.55 (dd, J=6.9, 1.2 Hz, 2H); ^{13}C NMR (101 MHz, $CDCl_3$) δ: 149.58, 149.35, 145.91, 144.48, 141.56, 141.52, 141.29, 140.58, 133.93, 133.40, 128.95, 128.58, 127.39, 127.25, 127.23, 126.74, 126.49, 126.32, 123.73, 123.31, 122.92, 122.87, 119.83, 119.60, 118.70, 117.49, 65.96. HRMS calcd for $C_{60}H_{36}$ 756.2817, found 756.2859.

Supporting Information The thermogravimetric analysis (TGA) curves, the differential scanning calorimetry (DSC) curves, the electroluminescence spectra, the material structures related to the device, the ^{1}H NMR and ^{13}C NMR spectra, the electrochemical properties and thermal properties, the crystal data and structure refinement of 1,4-SBF-Nap and 1,8-Oct-Nap and Cartesian coordinates of optimized molecules. The Supporting Information is available free of charge via the Internet at http://sioc-journal.cn.

References

[1] Baldo, M. A.; O'Brien, D. F.; You, Y.; Shoustikov, A.; Sibley, S.; Thompson, M. E.; Forrest, S. R. *Nature* **1998**, *395*(6698), 151.

[2] Pu, Y.-J.; Nakata, G.; Satoh, F.; Sasabe, H.; Yokoyama, D.; Kido, J. *Adv. Mater.* **2012**, *24*(13), 1765.

[3] Cui, L.-S.; Dong, S.-C.; Liu, Y.; Li, Q.; Jiang, Z.-Q.; Liao, L.-S. *J. Mater. Chem. C* **2013**, *1*(25), 3967.

[4] Tao, Y.; Yang, C.; Qin, J. *Chem. Soc. Rev.* **2011**, *40*(5), 2943.

[5] Quinton, C.; Thiery, S.; Jeannin, O.; Tondelier, D.; Geffroy, B.; Jacques, E.; Rault-Berthelot, J.; Poriel, C. *ACS Appl. Mater. Interfaces* **2017**, *9*(7), 6194.

[6] Maheshwaran, A.; Sree, V. G.; Park, H.-Y.; Kim, H.; Han, S. H.; Lee, J. Y.; Jin, S.-H. *Adv. Funct. Mater.* **2018**, *28*(36), 1802945.

[7] Poriel, C.; Rault-Berthelot, J.; Thiery, S.; Quinton, C.; Jeannin, O.; Biapo, U.; Tondelier, D.; Geffroy, B. *Chem.-Eur. J.* **2016**, *22*(50), 17930.

[8] Bai, Q.; Liu, H.; Yao, L.; Shan, T.; Li, J.; Gao, Y.; Zhang, Z.; Liu, Y.; Lu, P.; Yang, B.; Ma, Y. *ACS Appl. Mater. Interfaces* **2016**, *8*(37), 24793.

[9] Poriel, C.; Rault-Berthelot, J. *J. Mater. Chem. C* **2017**, *5*(16), 3869.

[10] Lin, N.; Qiao, J.; Duan, L.; Li, H.; Wang, L.; Qiu, Y. *J. Phys. Chem. C* **2012**, *116*(36), 19451.

[11] Lin, N.; Qiao, J.; Duan, L.; Wang, L.; Qiu, Y. *J. Phys. Chem. C* **2014**, *118*(14), 7569.

[12] Cui, L.-S.; Xie, Y.-M.; Wang, Y.-K.; Zhong, C.; Deng, Y.-L.; Liu, X.-Y.; Jiang, Z.-Q.; Liao, L.-S. *Adv. Mater.* **2015**, *27*(28), 4213.

[13] Shao, J.; Zhong, Y. *Chin. J. Org. Chem.* **2021**, *41*(4), 1447 (in Chinese).
(邵将洋; 钟羽武, 有机化学, **2021**, *41*(4), 1447.)

[14] Clarkson, R. G.; Gomberg, M. *J. Am. Chem. Soc.* **1930**, *52*(7), 2881.

[15] Zeng, W.; Lai, H.-Y.; Lee, W.-K.; Jiao, M.; Shiu, Y.-J.; Zhong, C.; Gong, S.; Zhou, T.; Xie, G.; Sarma, M.; Wong, K.-T.; Wu, C.-C.; Yang, C. *Adv. Mater.* **2018**, *30*(5), 1704961.

[16] Liu, H.; Liu, Z.; Li, G.; Huang, H.; Zhou, C.; Wang, Z.; Yang, C. *Angew. Chem., Int. Ed.* **2021**, *60*(22), 12376.

[17] Jiang, Z.; Yao, H.; Zhang, Z.; Yang, C.; Liu, Z.; Tao, Y.; Qin, J.; Ma, D. *Org. Lett.* **2009**, *11*(12), 2607.

[18] Jiang, Z.; Liu, Z.; Yang, C.; Zhong, C.; Qin, J.; Yu, G.; Liu, Y. *Adv.*

Funct. *Mater*. **2009**, *19*(24), 3987.
[19] Sicard, L. J.; Li, H.-C.; Wang, Q.; Liu, X.-Y.; Jeannin, O.; Rault-Berthelot, J.; Liao, L.-S.; Jiang, Z.-Q.; Poriel, C. *Angew*. *Chem*., *Int*. *Ed*. **2019**, *58*(12), 3848.
[20] Sicard, L.; Quinton, C.; Peltier, J.-D.; Tondelier, D.; Geffroy, B.; Biapo, U.; Métivier, R.; Jeannin, O.; Rault-Berthelot, J.; Poriel, C. *Chem*.-*Eur*. *J*. **2017**, *23*(32), 7719.
[21] Poriel, C.; Sicard, L.; Rault-Berthelot, J. *Chem*. *Commun*. **2019**, *55* (95), 14238.
[22] Poriel, C.; Rault-Berthelot, J. *Acc*. *Chem*. *Res*. **2018**, *51*(8), 1818.
[23] Dumur, F.; Bui, T.-T.; Péralta, S.; Lepeltier, M.; Wantz, G.; Sini, G.; Goubard, F.; Gigmes, D. *RSC Adv*. **2016**, *6*(65), 60565.
[24] Frisch, M. J.; Trucks, G. W.; Schlegel, H. B.; Scuseria, G. E.; Robb, M. A.; Cheeseman, J. R.; Scalmani, G.; Barone, V.; Petersson, G. A.; Nakatsuji, H.; Li, X.; Caricato, M.; Marenich, A. V.; Bloino, J.; Janesko, B. G.; Gomperts, R.; Mennucci, B.; Hratchian, H. P.; Ortiz, J. V.; Izmaylov, A. F.; Sonnenberg, J. L.; Williams; Ding, F.; Lipparini, F.; Egidi, F.; Goings, J.; Peng, B.; Petrone, A.; Henderson, T.; Ranasinghe, D.; Zakrzewski, V. G.; Gao, J.; Rega, N.; Zheng, G.; Liang, W.; Hada, M.; Ehara, M.; Toyota, K.; Fukuda, R.; Hasegawa, J.; Ishida, M.; Nakajima, T.; Honda, Y.; Kitao, O.; Nakai, H.; Vreven, T.; Throssell, K.; Montgomery Jr., J. A.; Peralta, J. E.; Ogliaro, F.; Bearpark, M. J.; Heyd, J. J.; Brothers, E. N.; Kudin, K. N.; Staroverov, V. N.; Keith, T. A.; Kobayashi, R.; Normand, J.; Raghavachari, K.; Rendell, A. P.; Burant, J. C.; Iyengar, S. S.; Tomasi, J.; Cossi, M.; Millam, J. M.; Klene, M.; Adamo, C.; Cammi, R.; Ochterski, J. W.; Martin, R. L.; Morokuma, K.; Farkas, O.; Foresman, J. B.; Fox, D. J. *Gaussian 16 Revision C.01*, Wallingford, CT, **2016**.
[25] Perdew, J. P.; Burke, K.; Ernzerhof, M. *Phys*. *Rev*. *Lett*. **1996**, *77*(18), 3865.
[26] Grimme, S.; Ehrlich, S.; Goerigk, L. *J*. *Comput*. *Chem*. **2011**, *32*(7), 1456.
[27] Weigend, F.; Ahlrichs, R. *Phys*. *Chem*. *Chem*. *Phys*. **2005**, *7*(18), 3297.
[28] Lu, T.; Chen, F. *J*. *Comput*. *Chem*. **2012**, *33*(5), 580.
[29] Humphrey, W.; Dalke, A.; Schulten, K. *J*. *Mol*. *Graph*. **1996**, *14*(1), 33.
[30] Yanai, T.; Tew, D. P.; Handy, N. C. *Chem*. *Phys*. *Lett*. **2004**, *393*(1), 51.
[31] Demeter, A.; Timári, G.; Kotschy, A.; Bérces, T. *Tetrahedron Lett*. **1997**, *38*(29), 5219.

(Fan, Y.)

